UNCOVERING THE ORIGINS OF SPIRAL STRUCTURE BY MEASURING RADIAL VARIATION IN PATTERN SPEEDS

SHARON E. MEIDT[1], RICHARD J. RAND[1], AND MICHAEL R. MERRIFIELD[2]
[1] Department of Physics and Astronomy, University of New Mexico, 800 Yale Blvd Northeast, Albuquerque, NM 87131, USA
[2] School of Physics & Astronomy, University of Nottingham, University Park, Nottingham, NG7 2RD, UK

ABSTRACT

Current theories of spiral and bar structure predict a variety of pattern speed behaviors, calling for detailed, direct measurement of the radial variation of pattern speeds. Our recently developed Radial Tremaine–Weinberg (TWR) method allows this goal to be achieved for the first time. Here, we present TWR spiral pattern speed estimates for M101, IC 342, NGC 3938, and NGC 3344 in order to investigate whether spiral structure is steady or winding, whether spirals are described by multiple pattern speeds, and the relation between bar and spiral speeds. Where possible, we interpret our pattern speeds estimates according to the resonance radii associated with each (established with the disk angular rotation), and compare these to previous determinations. By analyzing the high-quality H I and CO data cubes available for these galaxies, we show that it is possible to determine directly multiple pattern speeds within these systems, and hence identify the characteristic signatures of the processes that drive the spiral structure. Even this small sample of galaxies reveals a surprisingly complex taxonomy, with the first direct evidence for the presence of resonant coupling of multiple patterns found in some systems, and the measurement of a simple single-pattern speed in others. Overall, this study demonstrates that we are now in a position to uncover more of the apparently complex physics that lies behind spiral structure.

Key words: galaxies: individual (M101, IC 342, NGC 3938, NGC 3344) – galaxies: kinematics and dynamics – galaxies: spiral – galaxies: structure – methods: numerical

Online-only material: color figures

1. INTRODUCTION

The angular rate at which bar and spiral structures rotate, the pattern speed, is a parameter appreciated for its capacity to reveal information about the appearance, properties, and evolution of galaxy disks. Since the pattern speed determines the rate at which gas and stars encounter these structures, it provides a description of their influence on star formation, the processing of the interstellar medium (ISM), and the distribution of metals (e.g., Rand 1993; Knapen et al. 1996; Henry et al. 2003), for example, as well as the redistribution of mass in the disk. Bar torques depend on the pattern speed, and therefore gas inflow rates (Quillen et al. 1995) do, as well. In early-type barred galaxies, pattern speeds have also been used to investigate the central dark matter (DM) content in these systems (e.g., Debattista & Sellwood 2000; Corsini 2008; but see Dubinski et al. 2009).

The pattern speed moreover supplies a fundamental characterization with which to investigate the origin and evolution of large-scale structures, one of the prime unresolved issues in the dynamics and evolution of galaxy disks. With knowledge of bar and spiral or the radial variation of spiral pattern speeds in a given galaxy, it is possible to determine whether spiral structure is steady or winding, the domain and number of patterns that can be sustained in a disk, and the relation between bar and spiral pattern speeds. Direct pattern speed measurements, however, have been elusive.

Although grand-design spirals have been observationally linked to the presence of bars or companions (Kormendy & Norman 1979), it remains unclear whether spirals are long-lived density waves persisting over many revolutions (i.e., Lin & Shu 1964; Bertin et al. 1989), or rapidly evolving, transient features, as found in several simulations (Sellwood & Carlberg 1984; Thomasson et al. 1990; Sellwood & Kahn 1991).

It is also uncertain how waves can exist over large fractions of a disk radius, as observed. Since the resonances (inner and outer Lindblad; ILR and OLR) between which waves are expected to propagate in general do not span a large range in radius, waves of different speeds and structure may occupy distinct radial zones (Masset & Tagger 1997b). In barred galaxies, the apparent alignment between bar and spiral (as in M83, where the two-armed spiral emanates from the bar ends), initially taken as evidence for a common pattern speed, does not occur in general (Sellwood & Sparke 1988). Furthermore, where the bar ends near its corotation resonance (CR; e.g., as found in early types; Corsini 2008), a spiral generated with the same speed would lie mostly outside the CR (i.e., with dust lanes along the convex side of the arms), which is also uncommon.

In the theory of "mode coupling" (Sygnet et al. 1988; Masset & Tagger 1997b), multiple patterns in different radial zones are linked, such that the resulting wave structure can extend over a larger radial range than is possible for a single pattern. In this scenario, the CR of an inner pattern overlaps with the ILR of an outer pattern, and at this overlap energy and angular momentum are efficiently transferred outward in the disk. This was first demonstrated between simulated bars and spirals by Masset & Tagger (1997b) and later by Rautiainen & Salo (1999), who find, in addition, that other resonance overlaps, such as the coincidence of the spiral's inner 4:1 resonance with the bar CR, are also effective. Given that the radial extent of resonant orbits can be quite large, these overlappings can be spatially broad, and frequency diagrams can therein be suitably revealing. However, not all such resonance overlaps are accompanied by signs of true mode coupling (i.e., boosted beat modes detectable in simulation power spectra at the overlap; Masset & Tagger 1997b).

Spiral–spiral mode coupling may also occur, typified, perhaps, by the transition commonly observed between a strong two-armed spiral and more complex structure at some radius.

In their simulations, Rautiainen & Salo (1999) find evidence for spiral structure in the absence of a bar, spiral–spiral mode coupling, and multiple pattern speeds without mode coupling.

To observationally investigate these possibilities, we have undertaken a project to measure spiral pattern speeds and their radial variation using the Radial Tremaine–Weinberg (TWR) method developed by Merrifield et al. (2006), subsequently tested on simulations (Meidt et al. 2008a; hereafter Paper I), and recently applied to a real spiral in the grand-design galaxy M51 (Meidt et al. 2008b; hereafter Paper II). Like its traditional counterpart—the TW method for measuring a single, constant pattern speed (Tremaine & Weinberg 1984)—the TWR calculation yields measurements of pattern speeds using observationally accessible quantities based on a requirement of continuity. The method is direct, and so overcomes several of the obstacles in reliably estimating pattern speeds with other, indirect methods (e.g., resonance identification or modeling; Elmegreen et al. 1989, 1996; Rautiainen & Salo 2005; Garcia-Burillo et al. 1993).

Moreover, the TWR method provides a resolution for those applications of the TW method where pattern speed estimates show a clear, systematic departure from a single value (e.g., Zimmer et al. 2004; Merrifield et al. 2006). Particularly in disks with multiple or extended structures, this behavior implies that the pattern speed is not constant either because it varies temporally or spatially. By allowing the pattern speed to vary in the radial direction, the TWR method explicitly allows for the possibility that a galaxy may contain a number of distinct features at different radii, such as bars and spiral arms, each with their own pattern speeds. It also makes possible the detection of spiral winding and hence the estimation of the lifetime of a galaxy's current pattern.

Our aim with this paper is to expand to a larger sample of galaxies the TWR analysis recently applied to the grand-design spiral galaxy M51 (Paper II). Here, as there, we apply the method according to the prescription outlined in Paper I. The calculation employs regularization, which smooths otherwise intrinsically noisy solutions through the use of a prior models of the radial dependence of the pattern speed, and affords straightforward tests for bar–spiral and spiral–spiral relations, and spiral winding.

Also as in Paper II, for use as a kinematic tracer we consider observations of the ISM, which have become the standard choice of spiral tracer for meeting the continuity requirement of the method. The application of the TW and TWR methods to CO and H I observations of spiral galaxies (e.g., Westpfahl 1998; Rand & Wallin 2004; Merrifield et al. 2006) avoids significant problems with the stellar component in these systems, namely, the faintness of the old stellar disk, and the effects of star formation and obscuration by dust in spiral arms by which the application of the continuity equation is invalidated.

Furthermore, where the ISM is dominated by either the molecular (traced by CO) or atomic gas phases, conversion among phases can be assumed to occur at low levels on orbital timescales such that, together with the low true efficiency of star formation in spirals, the dominant component arguably obeys continuity (e.g., Zimmer et al. 2004; Rand & Wallin 2004). In addition, as an improvement on previous ISM-based TW spiral studies, here we analyze both molecular gas observations from the BIMA SONG (Helfer et al. 2003; maps include zero-spacing flux information) and archival 21 cm emission data tracing the atomic hydrogen phase. (The flux information at the largest scales in all of the H I cubes considered here is comparable to that achieved with single-dish observations; see references in Sections 2.2–2.5.) Our consideration of both CO and the more extended H I here serves two main purposes. In galaxies that are not molecule-dominated over the extent of the detectable CO emission, the H I supplements H_2 to establish a total particle, continuity-obeying tracer. The radial range of detectable pattern speeds is also increased in this way.

Part of our treatment, in this case, entails an investigation (where possible) into the sensitivity of TWR solutions to the CO-to-H_2 conversion factor X adopted in combining the data, which has been suggested to vary linearly with metallicity (e.g., Boselli et al. 2002). Following Zimmer et al. (2004) and Paper II, we consider the effect of variation in X with radius (but not the possibility, for example, of arm–interarm variations). We also take into consideration distortions or warps observable in the outer H I disks in our sample (described in Sections 2.1–2.5), which violate of one of the main TW assumptions (namely, that the disk is flat; Tremaine & Weinberg 1984).

Based on the a priori models described in Section 3.1, the best-fit pattern speed solutions calculated for each galaxy are presented in Sections 3.2–3.5. There, the resonances associated with each, which we identify through comparison with angular rotation curves, serve as a main informant of our results; our findings are motivated by, and compared with, the large body of work linking resonances to the dynamics and morphology of disks. We also discuss the limitations and sensitivities of the TWR calculation (described in Paper I) as applied to each galaxy and summarize our results in Section 4.

2. THE SAMPLE

2.1. Selection and Overview

In the following subsections, we describe the four spiral galaxies analyzed in this paper: M101, IC 342, NGC 3938, and NGC 3344. This small sample is not meant to be representative of variations in spiral structure with galaxy classification type, or to embody all possible theories of spiral structure. These nearby galaxies were selected simply for their clear spiral structure and moderate inclination, as well as for the availability of observations (specifically, both CO and H I in three of the four cases) of sufficient sensitivity and resolution to allow structure to be resolved and the radial variation of Ω_p to be investigated; see Paper I.

With this sample we explore three scenarios for applying the TWR method to observations of the ISM. We first consider both the molecular and atomic components of the ISM in M101, which is molecule-dominated over the detectable extent of the CO emission, and investigate whether there exists a relation between the speeds of the multiple structures apparent throughout the disk. We then apply the method to two galaxies (IC 342 and NGC 3938) where the ISMs are dominated by neither the atomic or molecular gas phases in the central few kpc; in this case, considering the total column density is necessary for meeting the continuity requirement of the method. Lastly, for NGC 3344, where the ISM is dominated by the atomic phase over the majority of the disk area (see Section 2.5), we analyze H I data alone, and with our TWR solution predict a pattern speed for the small bar.

In three of the four cases, a warp-like distortion is evident in the H I distribution and kinematics, often with little further evidence of a strong spiral pattern. A warp in the outer disk, characterized by position and/or inclination angles that
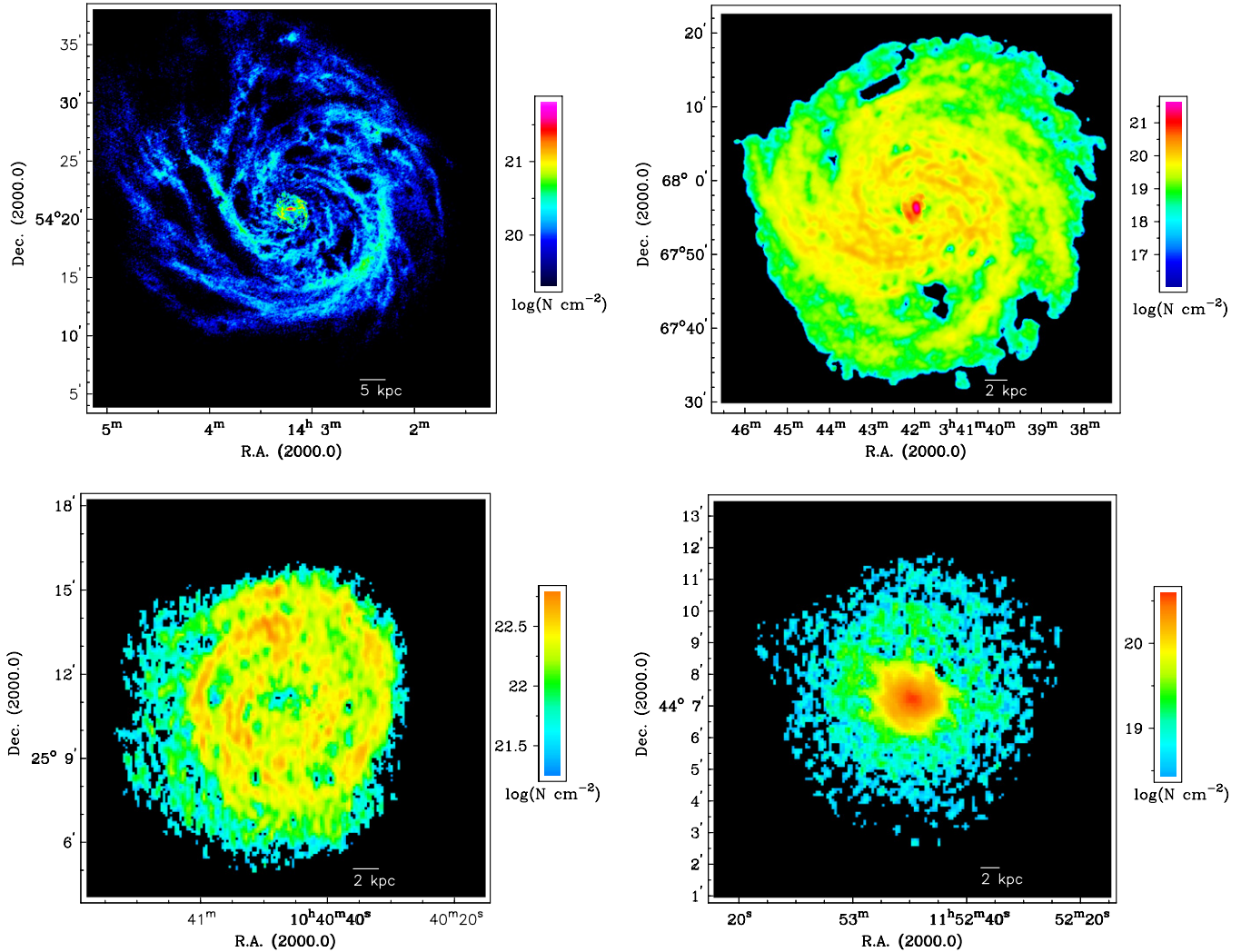
Figure 1. Clockwise from the top left: zeroth-moment maps for M101, IC 342, NGC 3938 (made from the combined CO and H I cubes), and NGC 3344 (made from the H I cube) showing the logarithm of the column density N in units of cm^{-2}. The horizontal bar near the bottom indicates the physical scale.
(A color version of this figure is available in the online journal.)

differ from those values in the disk interior, violates the TW assumption that the disk is flat (Tremaine & Weinberg 1984). In implementing the regularized TWR method, we therefore adopt the procedure advocated in Paper I (see the beginning of Section 3.1), which accommodates for the presence of information about the warp in the TWR quadrature by excluding it from regularized solutions.

Zeroth- and first-moment maps for each galaxy are shown in Figures 1 and 2. For M101, IC 342, and NGC 3938, these maps were generated from the combined CO and H I cubes, which were regridded to a uniform channel width and coadded in units of particles cm^{-2}. Prior to combination, the CO cubes were smoothed to the resolution of the H I and CO intensities converted to molecular column densities assuming a constant CO-to-H$_2$ conversion factor $X = 2.0 \times 10^{20}$ cm^{-2} (K km s^{-1})$^{-1}$, the Galactic mean value (e.g., Hunter et al. 1997). (Subsequent variations in the X-factor are considered when applicable.)

Tilted ring fits to the velocity field of the four galaxies were performed using the GIPSY (van der Hulst et al. 1992) task ROTCUR in order to derive the kinematic parameters used in the TWR calculation. For these fits, the systemic velocity is initially fixed to the value given in the literature, while the kinematic center, position angle (P.A.), and inclination are allowed to vary.

(The value and the errors on $V_{\rm sys}$ were subsequently determined by fitting with all other best-fit parameters held fixed.) The values we find are in good agreement with those nominally adopted for each galaxy and are listed in Table 1.

For the purposes of identifying resonances (corotation, inner and outer Lindblad), we also derived the circular velocity in each ring with the best-fit kinematic parameters held fixed. In each galaxy, these velocities are modeled in the unwarped portion of the disk with least-squares fits to the standard three-parameter approximation (i.e., Faber & Gallagher 1979):

$$V_{\rm rot}(r) = \frac{V_{\max}(r/r_{\max})}{(1/3 + 2/3(r/r_{\max})^n)^{3/2n}}, \qquad (1)$$

as shown in Figure 3. The error bars on each measured velocity there reflect the average deviation from this value on either the approaching or receding side, which together we find better represent the uncertainty in the rotation curve than do the formal errors returned by ROTCUR. With the fitted velocities, we then generate a set of smooth curves for Ω, $\Omega \pm \kappa/2$, and $\Omega \pm \kappa/4$; these curves are intended to reduce the impact of nonaxisymmetric motions (e.g., spiral streaming) on our resonance identifications and were invoked without regard to specific mass component characterization.
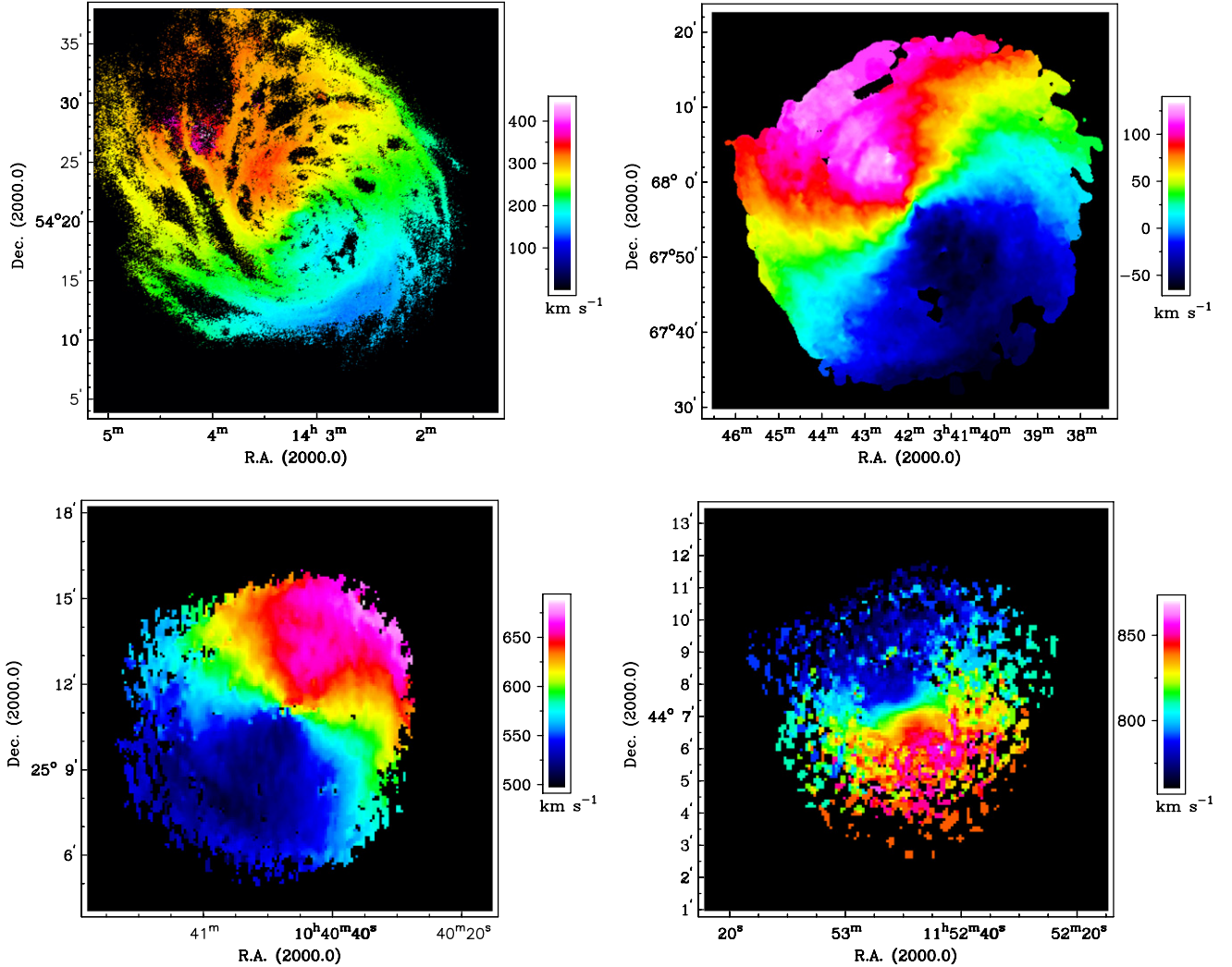
Figure 2. Clockwise from the top left: first-moment maps for M101, NGC 3938, IC 342 (made from the combined CO and H I cubes), and NGC 3344 (made from the H I cube) in units of km s^{-1}.

(A color version of this figure is available in the online journal.)

Table 1
Parameters Used in the TWR Calculation

Parameter	M101	IC 342	NGC 3938	NGC 3344
Dynamical center R.A. (α) (J2000)	$14^h3^m13\overset{s}{.}13$	$3^h46^m48\overset{s}{.}4$	$11^h52^m49\overset{s}{.}8$	$10^h43^m31\overset{s}{.}5$
Dynamical center DEC (δ) (J2000)	$54°20'56''$	$68°5'47\overset{''}{.}8$	$44°7'11\overset{''}{.}7$	$24°55'18\overset{''}{.}3$
Distance (Mpc)	7.4	2.0	11.3	6.9
Systemic velocity (V_{sys}, km s^{-1})	244 ± 8	30 ± 2	809 ± 3	586 ± 3
Position angle (°)	42 ± 3	42 ± 3	21 ± 2	155 ± 2
Inclination (°)	21 ± 6	31 ± 5	14 ± 3	25 ± 4

Notes. Entries for the dynamical center, inclination, and position angle for each galaxy were derived with a tilted ring analysis of the first moment of the data cube using the GIPSY task ROTCUR. Optimal values for the distance originate with references cited in Sections 2.2–2.5.

2.2. M101

This SABcd galaxy ($D = 7.4$ Mpc; Jurcevic & Butcher 2006) is an excellent candidate for analysis with the TWR method. The molecular gas filling the central 3′ hole in the H I emission features a bar discovered by Kenney et al. (1991). The bar is a clear candidate-driver of the spiral structure that appears to emanate from the bar region. At the outer radii, tidal interaction with companion galaxies (e.g., NGC 5474 and NGC 5477; Huchtmeier & Witzel 1979; Waller et al. 1997) is thought to be responsible for the lopsidedness and distortion in the H I

distribution, and may also be the source of the spiral (Waller et al. 1997). The high resolution (∼7′′) of the total H$_2$+H I maps constructed from the BIMA SONG CO data and THINGS H I data (with ROBUST weighting scheme; Walter et al. 2008) allows us to apply the TWR method with exceptional leverage on the radial dependence of the pattern speed throughout the disk. We aim to derive the bar and spiral pattern speeds, and identify multiple spiral modes and spiral winding, if present.

As considered in the upcoming discussion (Section 3.2), we note that the rotational velocities between $r \sim 7$ and 14 kpc and at radii $r \gtrsim 19$ kpc in the top right of Figure 3 are not well
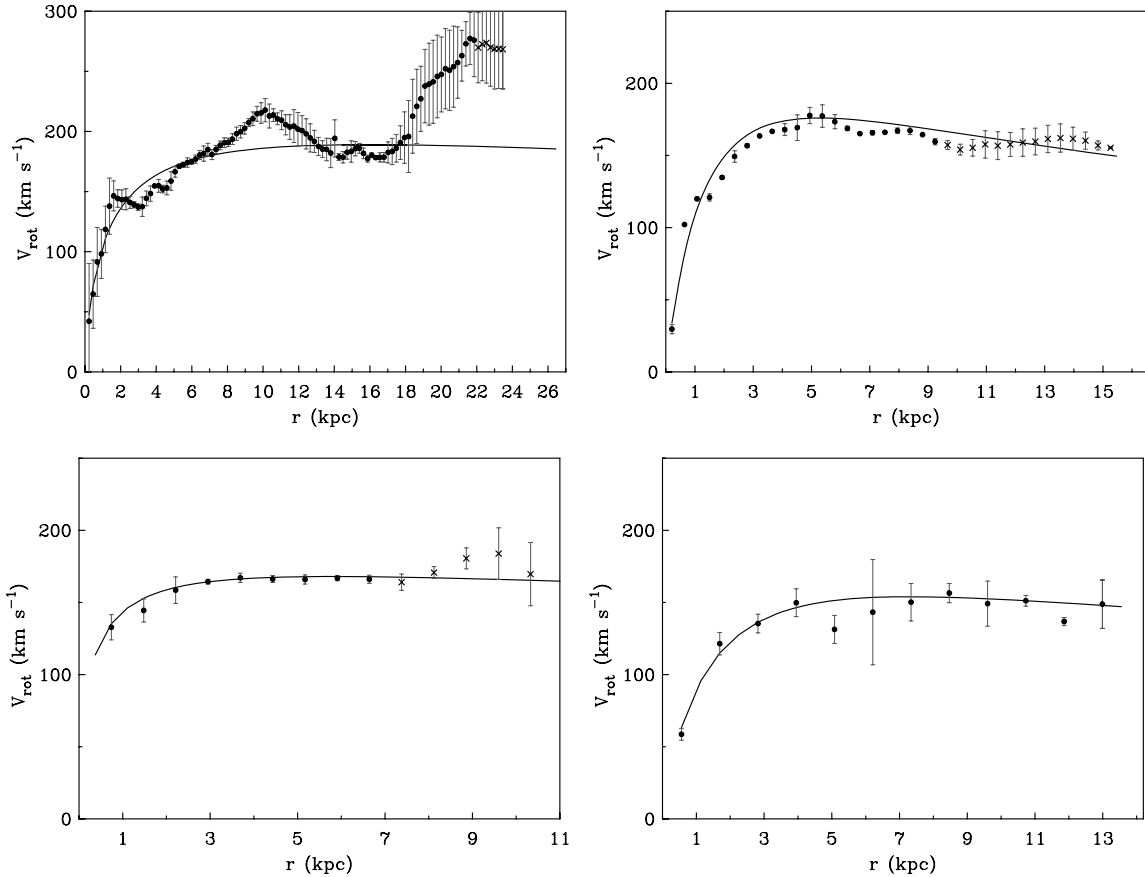
Figure 3. Clockwise from the top left: rotational velocities for M101, IC 342, NGC 3938, and NGC 3344. Values measured with tilted ring fits to the velocity fields shown in Figure 2 with all optimal parameters listed in Table 1 held fixed are shown as filled circles (crosses) in the unwarped (warped) region of the disk (as identified in Sections 3.2–3.5). The points are shown spaced at the resolution of each map with error bars (shown in dark gray) representing the average variation in the derived velocity from side to side (approaching and receding). The solid line in the plots for M101, IC 342, and NGC 3938 is the least-squares fit of the velocity model (Equation (1)) to the velocities measured in the unwarped portion of the disk (filled circles), with best-fit parameters: $V_{max} = 189$ km s^{-1}, $r_{max} = 15.89$ kpc, $n = 0.43$ for M101; $V_{max} = 167$ km s^{-1}, $r_{max} = 5.62$ kpc, $n = 0.76$ for IC 342; $V_{max} = 154$ km s^{-1}, $r_{max} = 7.3$ kpc, $n = 0.76$ for NGC 3938; $V_{max} = 168$ km s^{-1}, $r_{max} = 5.8$ kpc, $n = 0.29$ for NGC 3344. (For NGC 3344, to achieve an accurate fit these parameters had to be constrained a priori to a range that best reproduces the flatness for $r \gtrsim 3$ kpc.) All solid lines are used to derive the smoothed angular rotation and resonance curves presented in Sections 3.2–3.5.

fit here. Also, while the rise in the latter zone appears on both the approaching and receding sides, a $\sim$75 km s^{-1} asymmetry exists therein.

In addition, as demonstrated by Wong & Blitz (2002) assuming $X = 1.8 \times 10^{20}$ cm^{-2} (K km s^{-1})$^{-1}$ (slightly lower than our adopted value), and using the BIMA SONG data we analyze here, the ISM is molecule-dominated over the extent of the CO emission. However, the disk is known to sustain a metallicity gradient, which, for a linear dependence of X on metallicity (e.g., Boselli et al. 2002), could imply variation in X with radius. So, while a constant offset should have no implications for TWR solutions, we also consider the effect of variation in X outward from the center.

2.3. IC 342

For this Seyfert SABcd galaxy ($D = 2.0$ Mpc; Crosthwaite et al. 2000), we base our analysis on the BIMA SONG CO data cube and the 38″ VLA H I observations first published by Crosthwaite et al. (2000). As in M101, the CO fills the central hole in H I distribution, but here the atomic gas makes a significant contribution to the total gas density before the edge of the CO emission. A thorough discussion of the H I–CO overlap and the features (a bar, a two-armed spiral, and a four-armed spiral) in the two gaseous components can be found in the study of Crosthwaite et al. (2001).

2.4. NGC 3938

NGC 3938 ($D = 11.3$ Mpc; Jimenez-Vicente et al. 1999) is a nearly face-on, late-type (SAc) galaxy exhibiting a central two-armed spiral that branches into multi-armed structure in the optical. The two strong spiral arms are evident in the molecular gas, which reaches a surface density comparable to that of the H I inside the edge of the CO emission. But where the stellar disk exhibits flocculent, but clear, spiral structure (with as many as six arms; Elmegreen et al. 1992), the H I disk is characterized by less well-organized, irregular structure. The combination of archival WSRT H I data with BIMA SONG CO observations establishes a total H$_2$+H I kinematic tracer at roughly 20″ resolution that extends to just beyond the optical extent of this galaxy (van der Kruit & Shostak 1982).

2.5. NGC 3344

The application of the model-independent TWR method to this H I-dominated, isolated SABbc galaxy ($D = 7.4$ Mpc; Verdes-Montenegro et al. 2000) should, in principle, clearly establish the relation of the ring-like morphological features at $r = 1$ kpc and $r = 7$ kpc, identified by Verdes-Montenegro et al. (2000) in optical images, to the large-scale patterns present in the disk (and their resonances). The outer ring, in particular, although thought unlikely to be related to the small bar (not
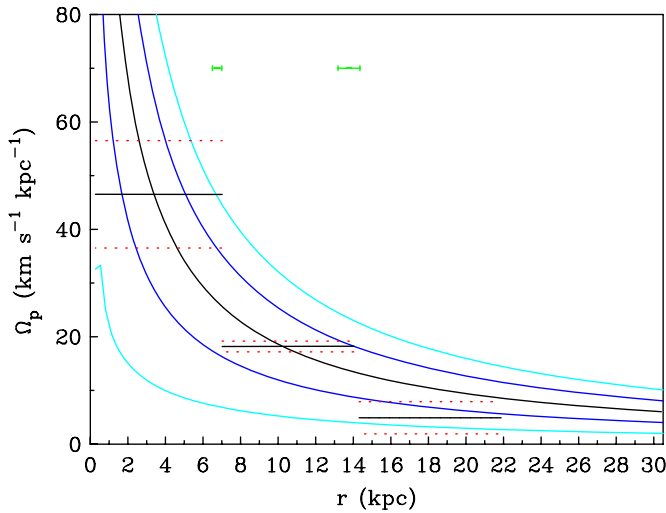
Figure 4. Best-fit regularized solution for M101 with $r_c = 21.9 \pm 0.43$ kpc for P.A. $= 42° \pm 3°$. For this solution, bins exterior to r_c (not shown) have been calculated without regularization. Dashed red lines represent the dispersion in solutions derived with a three-pattern speed model at P.A. $= 39°$ and $45°$. Horizontal error bars represent the dispersion in $r_{t,1}, r_{t,2}$, and r_c from P.A. to P.A. The innermost speed corresponds to $\Omega_{p,1} = 47 \pm 10$ km s^{-1} kpc^{-1} out to $r_{t,1} = 6.7 \pm 0.25$ kpc, followed by $\Omega_{p,2} \sim 18 \pm 1$ km s^{-1} kpc^{-1} out to $r_{t,2} = 13.8 \pm 0.58$ kpc and $\Omega_{p,3} = 5 \pm 3$ km s^{-1} kpc^{-1} out to r_c. Curves for Ω, $\Omega \pm \kappa/2$ and $\Omega \pm \kappa/4$ (see the text) are shown in black, cyan, and blue.

(A color version of this figure is available in the online journal.)

observed in the gas) with $a_B \sim 0.7$ kpc (Verdes-Montenegro et al. 2000), has not been otherwise conclusively related to the spiral. In search, as well, of spiral winding and multiple spiral modes, here we analyze 20″ resolution archival WSRT H I data where the dominant two-armed spiral and the outer ring are clear, in addition to the outer lopsided region exhibiting a twist in the isovels (van der Kruit & Shostak 1982). The zone of the bar and the inner ring, which falls within the central 26″ where there is little 21 cm emission, corresponds to less than two resolution elements. So although the ring is resolved in CO (Regan et al. 2002), and the peak H_2 column density (Helfer et al. 2003) there exceeds the H I, we do not consider the contribution of the molecular gas here.

3. RESULTS

3.1. Applying the TWR Method

We apply the regularized TWR method as in Paper I. For each galaxy, we consider several smoothed, testable models for $\Omega_p(r)$. These models vary as polynomials (order $n \lesssim 2$) designated into at most three distinct radial zones. Where a priori evidence suggests that there is little information from a strong pattern beyond a certain radius, or that the TW assumptions are otherwise violated by the presence of a warp, for example, our models also include the parameterization of a cut radius, r_c, beyond which all bins are calculated without regularization (i.e., the functional form is unconstrained). These models, with r_c marking the end of the dominant structure, have been demonstrated to sufficiently separate the compromised zones in the disk from regions where information about patterns can be reliably extracted in the TWR calculation (Papers I and II). All transitions r_t between distinct zones and all cut radii, where present, are treated as free parameters.

For each model, the two numerical solutions for $\Omega_p(r)$ from either side of the galaxy ($y > 0$ and $y < 0$; Merrifield et al.

2006) are averaged to construct a single, global model solution. Each model solution is then judged based on a simple reduced χ^2 statistic, with the best-fit solution corresponding to the χ_ν^2-minimum in the full parameter space.

As in Paper II, the random, measurement errors used in the regularized calculation, and with which we judge the best-fit solution, reflect uncertainty arising with the chosen flux cutoff in the first-moment maps. The systematic errors on each measurement represent uncertainty in the P.A., which is the dominant source of error in TW and TWR estimates (Debattista 2003; Paper I), roughly 20% for $\delta_{P.A.} = 3°$. But, here we report these as a dispersion on each measured value, rather than present individual solutions for each P.A; this is possible here since, unlike in M51 (Paper II), we find no meaningful evidence that the form of the model associated with the best-fit solution for any of the galaxies in the current sample varies from P.A. to P.A. Also, unless otherwise noted, errors due to uncertainty in, e.g., the inclination angle are generally smaller and are not reported; these prove to be of little consequence to the accurate placement of radial bins defined in the quadrature (as suggested in Paper I). The additional change introduced in the measurements Ω_p through a change in $\sin i$ is furthermore shared by Ω and κ, and so our resonance identifications, in particular, should not be effected by error in the inclination to first order. A thorough account of our methodology can be found in Paper I (and references therein).

3.2. M101

We apply the TWR calculation with radial bin width $\Delta r = 7″ = 0.27$ kpc ($D = 7.4$ Mpc), the resolution of the combined cube. Together with the position of the outermost slice on each side, $|y| = 30.4 \cos i$ kpc, this establishes the extent of integration along each slice, equipping solutions with 113 bins in total. The best-fit solution given a P.A. uncertainty $\pm 3°$ is plotted in Figure 4. There shown, also, are the rotation and resonance curves derived as described in Section 2.1. It should be noted that a ~ 75 km s^{-1} asymmetry in the rotational velocities from the approaching and receding sides exists at radii $r \gtrsim 20$ kpc (e.g., Kamphuis 1993; Jog 2002).

The outermost portion of the disk is effectively removed from the solution with the parameterization of a cut radius $r_c = 21.9 \pm 0.43$ kpc. This radius, identified at the minimum of the χ^2, is comparable to the location where the disk becomes visibly distorted. We find that the outer distortion/lopsidedness clear in the surface density is well characterized by the predominance of an $m = 1$ asymmetry beyond $r \sim 20$ kpc in the Fourier decomposition (Figure 5) and also matched by a warp in the outer velocity field; in addition to the rotation curve asymmetry, with our ROTCUR analysis we find that the P.A. and inclination of fitted rings beyond this radius vary significantly from the nominal values established in rings interior. (We note that this strong variation in the P.A. is found to start at a much larger radius than identified by Rownd et al. 1994.) Inclination variation, in particular, is a violation of the TW/TWR assumptions and so we argue that, by excluding the bins covering the outer disk from models for $\Omega_p(r)$, the remaining, inner regularized bins are better equipped to reproduce the true pattern speed. (Note that with this cut radius a possible $m = 1$ mode describing the outer, lopsided portion of the disk is ignored.)

In this case, the most conspicuous aspect of the solution is the pair of transitions at $r_{t,1} = 6.7 \pm 0.25$ kpc and $r_{t,2} = 13.8 \pm 0.58$ kpc (marked in Figure 6) between three distinct
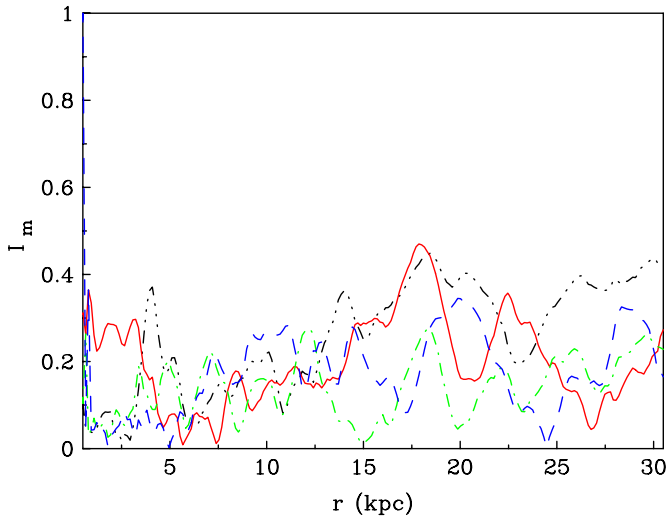
Figure 5. Fourier power spectrum of the zeroth-moment map shown in the top left of Figure 1. Modes up to $m = 4$ are plotted as a function of radius with lines for $m = 1$ in the black dash-dot-dot-dot, $m = 2$ in the red solid, $m = 3$ in the green dash-dot, and $m = 4$ in the blue dash.

(A color version of this figure is available in the online journal.)

Figure 6. Total $H_2 + H\,I$ surface density in M101 highlighting the structure inside ~ 18 kpc. The transitions $r_{t,1}$ and $r_{t,2}$ marking the extents of the first and second pattern speeds in our solution are shown as dashed white circles. The corotation radius $r_{CR} = 3.5$ of the innermost speed is shown as a solid white circle. The horizontal bar near the bottom left indicates the physical scale.

(A color version of this figure is available in the online journal.)

pattern speeds: $\Omega_{p,1} = 47 \pm 10$ km s^{-1} kpc^{-1}, $\Omega_{p,2} = 18 \pm 1$ km s^{-1} kpc^{-1}, and $\Omega_{p,3} = 5 \pm 3$ km s^{-1} kpc^{-1} out to r_c. As discussed below, the innermost, constant speed is nearly identical to the value $\Omega_p = 48 \pm 8$ km s^{-1} kpc^{-1} measured from the CO maps, alone (see Section 3.2.1), while the second pattern speed is consistent with the value generally upheld in the literature ($\Omega_p \sim 19$ km s^{-1} kpc^{-1} for $r_{CR} \sim 12$ kpc, e.g., Waller et al. 1997; but see the end of this section).

The quality of our measurement is especially clear in the precision with which the transitions between the three-pattern speeds are determined. The transition $r_{t,1}$, for example, shows less than 5% variation from P.A. to P.A. This transition coincides with a marked decrease in $m = 2$ power (Figure 5) and occurs well past the edge of the CO emission. We can therefore recognize that the inner speed describes the molecular bar and the two-armed spiral manifest in the CO and weakly traceable in H I, which Elmegreen et al. (1992) identify in the B band out to $r \sim 6$ kpc (estimated from their placement of the inner 4:1 circle in Figure 1, Plate 14, rather than with the discrepant value listed in Table 3 there). (Yet, we also note a four-armed appearance to the structure where spur-like features associated with either arm emerge, clear in CO emission and in the B band.)

This result, namely, that structure in H I shares the same pattern speed as the structure interior (exhibited solely by the molecular gas), admits a much stronger conclusion than can be drawn from the CO, alone. Our rotation and resonance curves indicate that the inner pattern ends near its OLR ($r \sim 7$ kpc; or possibly the outer 4:1 resonance, within the errors) which would not be evident from the application of the TWR method to CO data covering $r \lesssim 3.5$ kpc (corresponding to the central zone in Figures 1 and 6 with column density $\gtrsim 10^{20.6}$ cm^{-2}). This finding is consistent with the theoretical expectation for the forbidden propagation of spiral density waves beyond this resonance, which observations corroborate (see Elmegreen et al. 1989).

Likewise, corotation for this speed occurs at $r = 3.5$ kpc, very near the transition between molecular and atomic gas (see Figure 6). With its lack of clear structure and relatively low surface density, this location in the gaseous disk seems
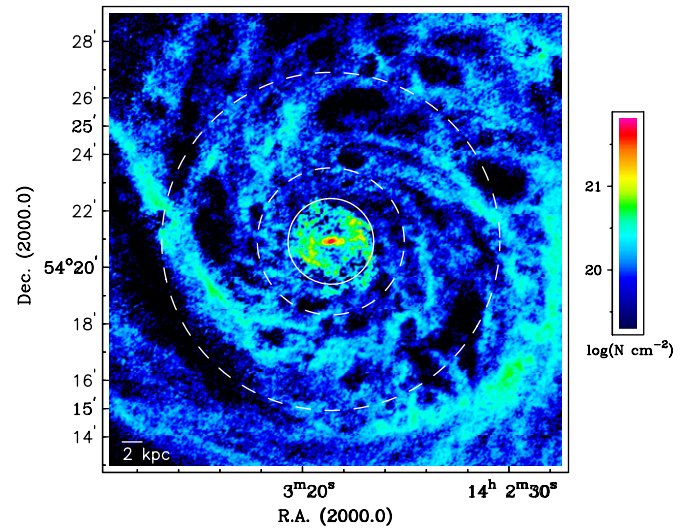
consistent with an expected depopulation near CR owing to opposing torques (whereby gas is driven inward between ILR and CR and outward between CR and OLR). (This impression, however, may be subject to the sensitivity of the CO map and the assumed X-factor.)

Interior to corotation, our determination of the disk angular rotation becomes less certain at a disadvantage to definitive resonance identifications. Nevertheless, the two-armed spiral exhibited near $r \sim 2$ kpc by the molecular gas—and which appears almost ring-like—is arguably located near the inner 4:1 resonance kpc, or UHR, where gas can accumulate on its path inward from corotation to ILR (Buta & Combes 1996). In addition, as will be discussed in more detail in Section 3.2.1, the central concentration of gas in the form of the molecular bar (with length ~ 1 kpc) appears to lie well within the CR. This is also true of the stellar bar with $a_b \sim 2$ kpc (Kenney et al. 1991), which suggests a scenario quite different from observational findings in favor almost exclusively of fast stellar bars (with $1 \lesssim r_{CR}/a_b \lesssim 1.4$; Corsini 2008), at least in early-type barred galaxies. Instead, the stellar bar here seems reminiscent of the slow bars found in the simulations of Combes & Elmegreen (1993) and Rautiainen et al. (2008).

As for the pair of pattern speeds $\Omega_{p,2}$ and $\Omega_{p,3}$ outside $r_{t,1} = 6.7 \pm 0.25$ kpc, we can similarly use the curves in Figure 4 to interpret their radial domains in terms of resonances. This is less straightforward, however, primarily because of our uncertainty in the poorly fit rotation curve here, as well as the complex nature of the spiral structure visible in the H I surface density, which is characterized by power in several Fourier modes (see Figure 5 and optically, Elmegreen et al. 1992). Notably, between $r \sim 6$ kpc and 13 kpc, the structure visible in H I appears four armed (see the top left panel in Figures 1 and 5). Meanwhile, near $r = 13$ kpc a two-armed pattern starts to predominate again, as indicated in Figure 1 and by Figure 5 where the power in the $m = 4$ mode decreases relative to the $m = 2$ mode.

In this case, the transition $r_{t,1}$ in Figure 4 would seem to associate the second speed $\Omega_{p,2}$ with the four-armed spiral, here found to extend between the inner and outer 4:1 resonances at

$r \sim 6.8$ kpc and $r \sim 14$ kpc. (This is unchanged even with rotation curve models where the rise and fall in velocities between $r = 8$ and 14 kpc in Figure 3 are more closely (yet coarsely) fit, although the end of $\Omega_{p,2}$ more nearly approaches Ω-$\kappa/2$.) The four-armed spiral in ESO 566-24 likewise extends between its inner and outer 4:1 resonances (Rautiainen et al. 2004). Our finding is also roughly consistent with the identification made by Elmegreen et al. (1992, in Figure 1, Panel 14 there), namely, that the zone dominated by the four-armed spiral is bounded by the inner 4:1 circle with $r \sim 6$ kpc and the CR circle with $r \sim 12$ kpc. (We would argue, however, that the end of this zone occurs past the CR, which we find near $r = 10$ kpc, depending on the rotation curve.)

This is a scenario moreover favored by our TWR solution in that the transition to the four-armed spiral occurs at a resonance overlap; where $\Omega_{p,1}$ ends at OLR, within the uncertainties, $\Omega_{p,2}$ begins near its inner 4:1 resonance at $r \sim 7$ kpc. Such an alignment of resonances, although not conclusively associated with mode coupling (i.e., as opposed to CR–ILR overlaps identified by Masset & Tagger 1997b), has been identified in the simulations of Rautiainen & Salo (1999) and Debattista et al. (2006), as well as in the grand-design spiral M51 through application of the TWR method (Paper II). Presumably, this overlap is characteristic of a physical mechanism by which spiral structure can be sustained over a large span in radius (Rautiainen & Salo 1999).

The transition $r_{t,2}$ between $\Omega_{p,2}$ and $\Omega_{p,3}$ may also be accompanied by resonance overlap: the outermost speed, which spans a radial domain well matched to that of the two-armed spiral within $12 \lesssim r \lesssim 20$ kpc (marked by the increase in $m = 2$ power in Figure 5), could begin at either the ILR or inner 4:1 resonance. Large fractional errors on $\Omega_{p,3}$, of course, make this identification particularly vague. Likewise, the end of this pattern, as designated by the cut radius, can be only indefinitely related to realistic resonances (e.g., CR; at least with our current determination of the angular rotation), although it is just beyond the end of the outer two-armed spiral identified by Elmegreen et al. (1992) near $r = 19$ kpc (again, according to their Figure 1, Panel 14, rather than Table 3). In addition, whether or not the resemblance to Ω-$\kappa/2$, Ω-$\kappa/4$, or Ω suggested in Figure 4 is significant remains unclear at this point, especially in light of the nearly linear rise (and the asymmetry) in the rotation velocities outside $r \sim 19$ kpc (not well modeled here; see Figure 3) suggesting that the angular rotation curve may flatten out near this radius. The values of Ω-$\kappa/2$ and Ω-$\kappa/4$ would be lower (and Ω+$\kappa/2$ and Ω+$\kappa/4$ higher) than in Figure 4, in which case $\Omega_{p,3}$ may coincide with Ω-$\kappa/4$.

Despite our uncertainty in the outermost speed, overall, the TWR solution presents compelling evidence for extensive spiral structure described by multiple pattern speeds that are moreover related by their overlap at resonance. Given that this galaxy is tidally interacting (e.g., as argued by Ideta 2002), our pattern speed solution may be suggestive of the scenario explored by Salo & Laurikainen (2000) in simulations of M51. Those authors find that waves of higher and higher pattern speeds are excited as tidally induced waves near Ω-$\kappa/2$ propagate inward. But considering that resonance overlap is not a feature in those simulations, our finding of a link between the speeds in M101 (and in M51; Paper II)—similar to the overlaps so far demonstrated between bars and spirals in simulation (e.g., Masset & Tagger 1997b; Rautiainen & Salo 1999)—may imply that at least the inner disk is dominated by internal, rather than external, effects. The speeds and structure within $r < r_c \sim 22$ kpc,

however, have yet to be related to the asymmetric remainder of the disk. If the outer warp is a lopsided, $m = 1$ mode, its pattern speed (not measured here) may be determined by, and reveal clues to, tidal encounter with the companion galaxies of M101.

3.2.1. The Inner Pattern Speed in M101

As stated previously, the inner disk appears to sustain only a single, constant pattern speed, $\Omega_{p,1} = 47 \pm 10$ km s^{-1} kpc^{-1}. This may be surprising, given the distinct bar pattern visible in the CO emission, which we might expect to end near CR and rotate with a pattern speed distinct from that of the spiral pattern immediately exterior. In order to determine whether our TWR solution is an accurate representation of the true speed, in this section we discuss the evidence in favor of only a single-pattern speed in this zone, consider whether the measurement is an artifact of variation in the X-factor, and make comparisons to findings in the literature.

For this investigation, we consider the CO data alone. As might be expected given the radial domains of the two-pattern speeds, we find that solutions calculated from the CO and H I maps, individually, supply pattern speed estimates nearly identical to those in either the inner or outer zones of the solution in Figure 4; the TWR result from the CO maps, $\Omega_p = 48 \pm 8$ km s^{-1} kpc^{-1}, is within the errors of the inner speed measured from the combined maps. Furthermore, the contribution made by the bar and inner spiral pattern in a given slice can be more easily identified when slices do not also contain information from throughout zone of the H I. (Note that, without the need for a cut radius, TWR solutions discussed below are all completely regularized.)

Of course, the notably low sensitivity of the CO map—with the interarm regions and the zone surrounding the bar showing little, if any, emission (Figure 6; see also Helfer et al. 2003)—itself raises significant doubts about whether the pattern speed can be accurately measured. According to Paper I, however, as it is engaged with the TWR calculation, regularization essentially attributes information within a given element of the TWR kernel to all elements at the same radius in all other slices, thereby compensating for zones which lack clear signatures of patterns. (Whether or not this is accurate depends primarily on how well the P.A. and inclination have been determined.) Errors that may be expected to arise in such low S/N regions are furthermore smoothly redistributed throughout the solution.

Given that the net result is an effective extraction of the available information, we argue that our regularized solution is a reliable indication that the data do not support the measurement of more than a single-pattern speed. In fact, when we impose a transition near the expected molecular bar end, solutions with 0.75 kpc $< r_t < 1.6$ kpc either indicate no difference between the inner and outer pattern speeds, or the inner speed is only slightly higher than, and within the errors of, the outer.

As evidence of the incompatibility of a distinct, higher pattern speed with the data, in Figure 7 we show a comparison between the $\langle v \rangle$ (defined in Paper II and references therein) reproduced by the best-fit, constant pattern speed solution and by two mock pattern speeds: one for the bar, $\Omega_b = 115$ km s^{-1} kpc^{-1} (chosen in order that the bar ends near CR) and one for the spiral, $\Omega_s = 48$ km s^{-1} kpc^{-1} (adopted from the value of the best-fit solution). There, the best-fit solution yields a significantly better fit to the data than the two speeds for slices inside $|y| \sim 1.0$ kpc.

This conclusion does not appear to depend on the P.A. or inclination, unlike in M51 where the radial variation in the
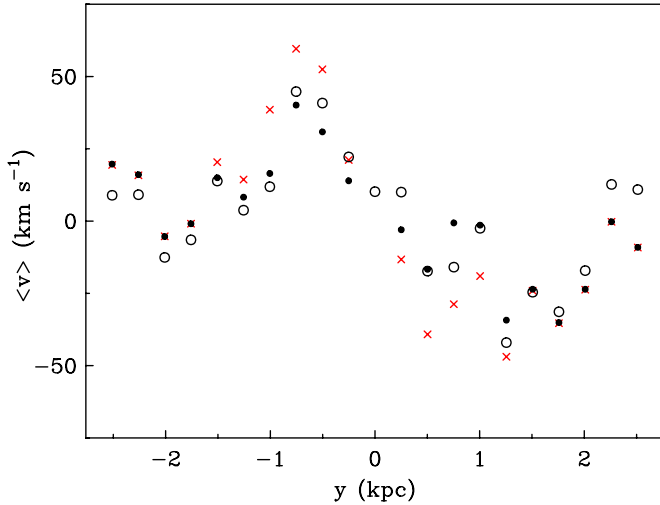
Figure 7. Plot of solution-reproduced (dots and crosses) and actual (open circles) integrals $\langle v \rangle_i = b_i / \int \Sigma dx$ (see Paper II) as a function of slice position y at P.A. $= 42°$ calculated from BIMA SONG CO data for M101. The values associated with the best-fit single-pattern speed solution (black dots) are plotted along with those of the two mock pattern speeds, $\Omega_{p,1} = 115$ km s^{-1} kpc^{-1} out to $r_t = 1.1$ kpc and $\Omega_{p,2} = 48$ km s^{-1} kpc^{-1} throughout the remainder of CO-traced disk (red crosses).

(A color version of this figure is available in the online journal.)

Figure 8. Best-fit regularized solution for IC 342 with $r_c = 9.8 \pm 0.19$ kpc for P.A. $= 42° \pm 3°$. For this solution, bins exterior to r_c (not shown) have been calculated without regularization. Dashed red lines and green horizontal error bars represent the dispersion in the pattern speeds and in r_t and r_c in solutions derived with a two-pattern speed model at the three P.A.s. The values in the zone of the bright spiral structure correspond to $\Omega_{p,1} = 38 \pm 7$ km s^{-1} kpc^{-1} out to $r_t = 5.7 \pm 0.71$ kpc and $\Omega_{p,2} = 11 \pm 6$ km s^{-1} kpc^{-1} out to r_c. Curves for Ω, $\Omega \pm \kappa/2$, and $\Omega \pm \kappa/4$ are shown in black, cyan, and blue.

(A color version of this figure is available in the online journal.)

best-fit solution varies from P.A. to P.A. (Paper II). For all angle combinations, a single, constant pattern speed yields a significantly better fit to the data than two, distinct speeds. Nor is the measurement sensitive to spatial variation in the CO-H$_2$ conversion factor. Based on the metallicity gradient -0.028 ± 0.01 dex kpc^{-1} measured from oxygen abundances (Cedres et al. 2004), we modeled an increase in X with radius across the CO emitting disk (according to the galaxy-to-galaxy scaling of Arimoto et al. 1996). In this case, a single, constant pattern speed is not only once again the best fit to the data, but at $\Omega_p = 53 \pm 6$ km s^{-1} kpc^{-1}, there is virtually no change to the measured value.

Our result, namely, that there is no distinct pattern speed over the length of the molecular bar, therefore seems to be authentic. Observations of H II regions downstream of the molecular spiral arms (Waller et al. 1997) also support our finding that the spiral arms lie inside corotation (although our spiral speed is much higher than the value inferred by Waller et al. 1997 from measurements of the difference in position of the H$_\alpha$ and CO emission). The relative spatial offset between the CO and UV emission in Figure 3 of Waller et al. (1997), while vague in places, seems sustained throughout the zone of the spiral and diminishes roughly near our CR radius. Since we find that the bar and spiral have the same pattern speed, this further implies that the bar ends well within its corotation radius.

This scenario has been suggested by Kenney et al. (1991) who, in first reporting on the 25° offset between the molecular and stellar bar position angles, noted a resemblance to the hydrodynamical simulations of Combes & Gerin (1985). Such a decoupled central gas concentration is found when the stellar bar is slow and drives spirals that develop inside corotation, as we suggest here.

A slow bar, ending well inside corotation, also seems to be reconciled with central DM content in M101 implied in the multicomponent simulations of Petitpas et al. (2004), which best reproduce the observed velocity field with a minimum disk. Where the DM contribution to the gravitational potential is large,
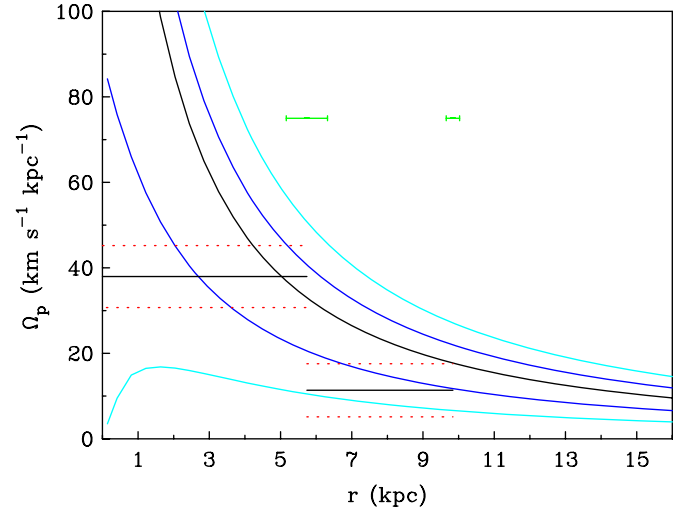
Debattista & Sellwood (2000) find that interaction between a bar and the DM halo through dynamical friction decelerates the bar (Weinberg 1985; Debattista & Sellwood 2000), such that it grows in length disproportional to the greater increase in r_{CR}. It should be noted, however, that the slowness of the bar implied in this case is a matter of debate (cf. Sellwood 2008, Dubinski et al. 2009, Weinberg & Katz 2007 who argue that slow bars are an artifact of the resolution of the N-body simulations used to model the interaction).

3.3. IC 342

The TWR calculation for this galaxy proceeds with the use of a radial bin width $\Delta r = 0.41$ kpc (as established by the resolution of the combined maps) using slices out to $|y| = 13.3$ kpc. The best-fit solution, plotted in Figure 8 together with angular rotation and resonance curves, measures two distinct pattern speeds inside the cut radius $r_c = 9.8 \pm 0.19$ kpc. As in M101, we find that this cut radius accurately reflects the location where the distortion/warp in the outer disk begins, e.g., as identified in the H I surface density/velocity field (Crosthwaite et al. 2000; see Figure 1).

Furthermore, the speed $\Omega_{p,1} = 38 \pm 7$ km s^{-1} kpc^{-1} inside $r_t = 5.7 \pm 0.7$ kpc is nearly identical to the value Crosthwaite et al. (2001) estimate based on their determination $r_{CR} = 4.2 \pm 0.7$ kpc from inspection of the field of velocity residuals. According to the solution in Figure 8, as parameterized by r_t this pattern terminates at either corotation (here at $r \sim 5$ kpc; conditional on the rotation curve, which is different from that of Crosthwaite et al. 2001) or OLR (within the uncertainties) in favor of the second, lower speed $\Omega_{p,2} = 11 \pm 6$ km s^{-1} kpc^{-1}.

The transition between the two speeds occurs very near where the spiral structure becomes visibly four armed (see Figure 9). This seems to establish that the outer arms are, in fact, best described by a speed that is distinct from that of the spiral interior, as previously suggested by Crosthwaite et al. (2000). Moreover, Figure 8 suggests a possible resonant link between
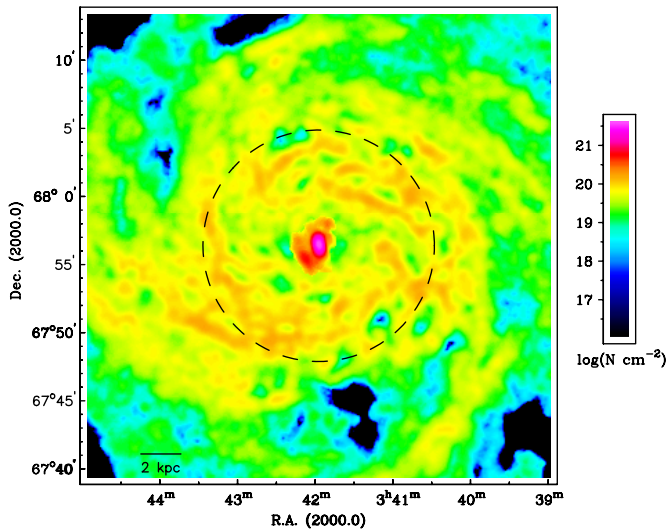
Figure 9. Total H_2+HI surface density in IC 342 highlighting the structure inside ~ 9.8 kpc. The transition r_t marking the extent of the inner pattern speed in our solution is shown as a dashed black circle. The horizontal bar near the bottom left indicates the physical scale.

(A color version of this figure is available in the online journal.)

Figure 10. Best-fit regularized solutions for NGC 3938 with P.A. $= 21° \pm 2°$. Dashed red lines for both solutions, Ω_p^A (thick line) and Ω_b^B (thin line) represent the dispersion in the pattern speeds at the three P.A.'s. The green horizontal error bar shows the dispersion from P.A. to P.A. in r_t in solutions derived with a two-pattern speed model. In the two speed solution, the value in the inner zone corresponds to $\Omega_{p,1}^B = 53 \pm 9.2$ km s^{-1} kpc^{-1} out to $r_t = 3.4 \pm 0.7$ kpc followed by $\Omega_{p,2}^B = 7.7 \pm 1.6$ km s^{-1} kpc^{-1}, while the single, constant speed solution measures $\Omega_p^A = 6.6 \pm 2.1$ km s^{-1} kpc^{-1}. Curves for Ω and $\Omega \pm \kappa/2$ are shown in black and cyan.

(A color version of this figure is available in the online journal.)

the two speeds in IC 342, in that the lower speed begins near its ILR (or possibly its inner 4:1 resonance). The low speed also seems to end at the 4:1 resonance, and possibly CR (within the uncertainties). However, the cut radius r_c in Figure 8 seems less an accurate bound on the four-armed spiral, which continues out to $r \sim 11$ kpc (see the zeroth-moment map in Figure 1), than an indication of where the warp begins. In this case, whether the warp and four-armed spiral are related or share a common origin is unclear.

Although we might also infer from Figure 8 that the inner speed lacks an ILR, our uncertainty in the rotation curve at the center is high, given the low resolution of the maps. Without more confidence in the behavior of the Ω-$\kappa/2$ curve, in particular, it remains unclear whether this speed, and the structure it describes, has an inner bound. Currently, then, both the spiral structure traced by CO and the distinct bar with length $a_B \sim 1.5$ kpc (Crosthwaite et al. 2000) appear to rotate with speed $\Omega_p \sim 40$ km s^{-1} kpc^{-1}. As in M101, this notably implies that the bar ends well inside its corotation radius, a circumstance which may also be evidenced by the $\sim 9°$ offset between molecular and stellar bar major axes (Crosthwaite et al. 2001), as similarly discussed in Section 3.2.1.

On the other hand, the molecular bar and the inner spiral could have different pattern speeds measurable, in principle, but for the width of the radial bins; information from the zone of the molecular gas, which covers a relatively small extent, is limited to only a minor contribution in solutions. Although the two-pattern speed solution in Figure 8 yields a significantly better fit to the data, a higher pattern speed can, in fact, be recognized in solutions modeled with three distinct pattern speeds: the lowest χ_ν^2 solution of this type at P.A. $= 42°$ favors a transition at $r_t^i = 1.6 \pm 0.45$ kpc from $\Omega_p = 34 \pm 9$ km s^{-1} kpc^{-1} to a higher $\Omega_p^i = 70 \pm 12$ km s^{-1} kpc^{-1}, with $\Omega_p = 12 \pm 4$ km s^{-1} kpc^{-1} between $r_t = 5.3 \pm 0.64$ kpc and $r_c = 9.8 \pm 0.19$ kpc. (Errors represent the dispersion in three-speed solutions where the inner-most transition, found best at the optimal P.A., is held fixed from P.A. to P.A.) This speed is particularly compelling since the bar would end very near CR, and at this radius overlap with the lower, spiral pattern's inner 4:1 resonance.
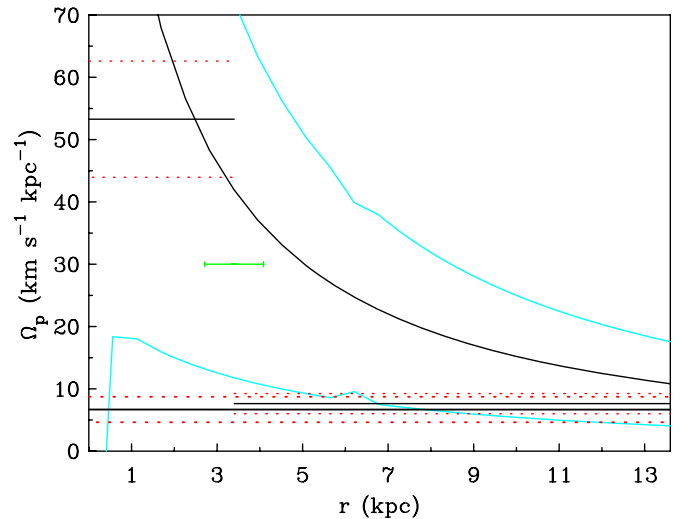
However, we emphasize that this identification is inconclusive at this point; the zone of the higher pattern speed is covered by only four radial bins, or less than 11% of the disk. (Note that the CO—which has a much higher resolution than the HI—alone cannot be used as a continuity-obeying kinematic tracer, unlike in M101.) Sensitivity to variation in the CO-to-H_2 conversion factor (e.g., given the metallicity gradient in this galaxy measured by Vila-Costas & Edmunds 1992) is also currently untestable; with such a large radial bin width any variation in X that we might accommodate would be crude at best and, with only four bins covering the CO emission, would likely yield an insignificant result.

3.4. NGC 3938

Given the resolution of the HI data (to which the BIMA CO cube had been smoothed prior to the combination) and, as a consequence, the rather large bin width $\Delta r = 1.7$ kpc, our TWR solutions calculated in slices $|y| \leqslant 13.1$ kpc contain only eight radial bins. This, together with the low inclination of the disk—which compromises the signatures of departures from axisymmetry in the velocity field—limits how well radial variation in the pattern speed can be detected, if present. Under this scenario, we find that two TWR solutions calculated with regularization over all radial bins (i.e., with no r_c) fit the data equally well. The first ascribes a single, constant pattern speed $\Omega_p^A = 6.6 \pm 2.1$ km s^{-1} kpc^{-1} to structure throughout the disk, while the second incorporates the measurement of a distinct, higher pattern speed $\Omega_{p,1}^B = 53 \pm 9.2$ km s^{-1} kpc^{-1} inside $r_t = 3.4$ kpc (in addition to the lower $\Omega_{p,2}^B = 7.7 \pm 1.6$ km s^{-1} kpc^{-1}).

The measurement of any pattern speed at all may be surprising, given the low inclination angle and the apparent lack of strong, organized structure in both the HI and (smoothed) CO emission analyzed here. Comparison with the rotation curves in Figure 10 greatly aids our interpretation of the measurements, although any conclusions that might be drawn are tenuous at
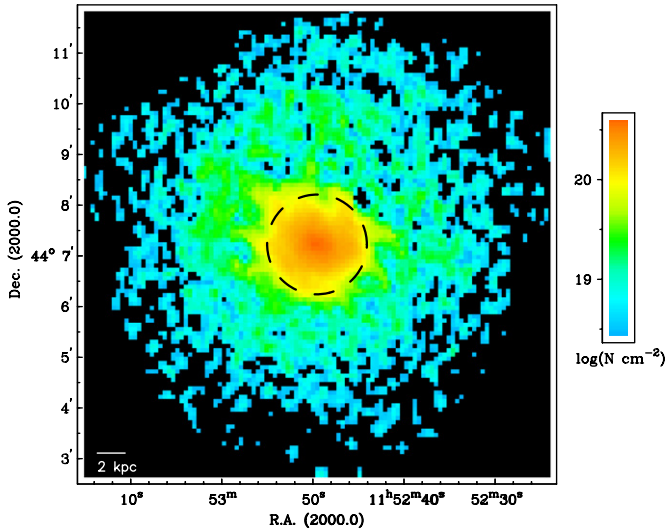
Figure 11. Total H_2+H I surface density in NGC 3938 highlighting the structure inside ∼15 kpc. The transition r_t marking the extent of the inner pattern speed in solution Ω_p^B is shown as a dashed black circle. The horizontal bar near the bottom left indicates the physical scale.

(A color version of this figure is available in the online journal.)

best; for this low inclination, rotation curves are highly uncertain (though similar to those throughout the literature, e.g., Jimenez-Vicente et al. 1999; Combes & Becquaert 1997).

With this in mind, we find it noteworthy that the low speed Ω_p^A (or $\Omega_{p,2}^B$) is very near Ω-$\kappa/2$ in the outer disk (Figure 10; and possibly near Ω-$\kappa/4$, as well). This similarity seems reminiscent of a pattern formed by closed, precessing elliptical orbits guided by the near-constancy of Ω-$\kappa/2$. But since there is no dominant $m = 2$ Fourier component visible in the 21 cm emission or in the NIR (as observed by Castro-Rodriguez & Garzon 2003) at these radii, it is unclear that this speed is associated with spiral structure, at all. A lack of spiral streaming motions in the atomic gas (as also observed in the ionized component of the ISM; Jimenez-Vicente et al. 1999) would furthermore lead us to expect that, for any asymmetry in the surface density, a value much closer to the disk angular rotation frequency Ω would be measured.

At radii $r \lesssim 6$ kpc, on the other hand, clear spiral structure is identifiable in the NIR (see the K-band image in Castro-Rodriguez & Garzon 2003). At the very least, this seems to suggest that the two-pattern speed solution Ω_p^B (with r_t as marked in Figure 11) may be more realistic than Ω_p^A; the faster inner speed seems more compatible with structure at these radii than $\Omega_p \sim 7$ km s^{-1} kpc^{-1} since, even with uncertainty in Ω at the inner radii and the near-constancy of Ω-$\kappa/2$ at the outer radii, the low pattern speed's ILR would lie at $r \gtrsim 5$ kpc.

Nonetheless, whether $\Omega_{p,1}^B$ is a reliable measurement of the expected higher pattern speed is difficult to assert. The transition r_t (see Figure 11) lies just inside the edge of the CO emission tracing a two-armed spiral (clear in the unsmoothed BIMA SONG map; Helfer et al. 2003), and so the measurement presumably reflects the speed of this pattern. However, even though this speed appears to cover a quarter of the disk, in general we expect that two radial bins would not supply sufficient leverage on the measurement. (This is arguably the reason why the two TWR solutions are indistinguishable.) Indeed, with so few bins in this zone we are prevented from diagnosing radial variation of order higher than zero. Furthermore, the accuracy of the measurement, if real, depends on how accurately infor-

mation about the two speeds can be separated according to the parameterization of the transition $r_t = 3.4$ kpc, which here may be severely limited by the size of the radial bin width. (Note that, as in IC 342, the unsmoothed 6″ resolution CO alone cannot be used as a continuity-obeying kinematic tracer, since ISM is not molecule-dominated over the extent of the CO emission. Tests for sensitivity to variation in the CO-to-H_2 conversion factor are also not well accommodated with so few, large radial bins.)

These shortcomings notwithstanding, the distinct measurement inside $r \sim 3$ kpc seems credible if only that it is consistent with values indicated by two independent approaches using different tracers of the spiral structure. Korchagin et al. (2005) find with a global modal approach that the dominant $m = 3$ and $m = 4$ modes in their multiwavelength observation-based simulations are well described with a pattern speed near ∼55 km s^{-1} kpc^{-1}. Martinez-Garcia et al. (2009) propose a similar pattern speed, ∼47 km s^{-1} kpc^{-1} (adopted from Martinez-Garcia et al. 2009 for $D = 11.3$ Mpc), based on the azimuthal age gradient across the spiral arms calculated from optical images.

From Figure 10, we might also argue that, within the uncertainties, $\Omega_{p,1}^B$ ends near corotation at $r_{CR} = 2.5$ kpc and so represents a physically realistic scenario, also recently identified in M51 (Paper II). However, this speed might just as reasonably end at OLR, depending on the rotation curve, the determination of r_t, and the measurement itself. Also, while this pattern appears to lack an ILR, this is uncertain given that the angular velocities are the least well determined at the inner radii. At this point, there also does not seem to be a clear relation between the two-pattern speeds (e.g., overlapping CR and ILR; Masset & Tagger 1997b), especially since resonances for the outer speed $\Omega_{p,2}^B$ are difficult to establish, given the flatness of the resonance curves.

While our confidence in the TWR measurement is tempered by the low inclination of the disk, the value of this analysis lies in the prospect of renewed perspective on the nature of the structure in this galaxy. Although in no way definitive (based on the TWR method, alone), the lower measurement near Ω-$\kappa/2$ (either Ω_p^A or $\Omega_{p,2}^B$), in particular, may be compatible with several pieces of evidence that point to the influence of the DM halo first contemplated by van der Kruit & Shostak (1982).

As investigated by Frenk et al. (1988) or by Jog (1997), for example, the DM halo may be responsible for the appearance of structure in this isolated galaxy, which otherwise seems difficult to reconcile with the finding that the gas disk is everywhere subcritical to gravitational instability (as remarked upon by Combes & Becquaert 1997, and aside from an alternative increase in instability possible through the coupling between multiple components in the system, e.g., Jog 1992).

Specifically, where the Toomre stability parameter in the gas is high, Bureau et al. (1999) and Frenk et al. (1988) suggest that the torque due to a triaxial halo (predicted by cold dark matter (CDM) simulations of hierarchical structure formation; e.g., Dubinski & Carlberg 1991) with slow figure rotation can drive structure in extended H I disks. Material (though not exclusive) to this scenario, the disk of NGC 3938 exhibits intrinsic ellipticity: as similarly diagnosed in other eccentric nearby spirals by Andersen et al. (2001), the photometric and kinematic position angles of NGC 3938 are offset by nearly 50° (Daigle et al. 2006). In fact, Castro-Rodriguez & Garzon (2003) measure an ellipticity $\epsilon_J = 0.11$ in the J band. So while the ellipticity may have arisen with an asymmetric accretion of matter, for example, it could also reflect an $m = 2$ potential perturbation occasioned by triaxiality in the DM halo (see, e.g., Andersen et al. 2001 and references therein). In this case, the
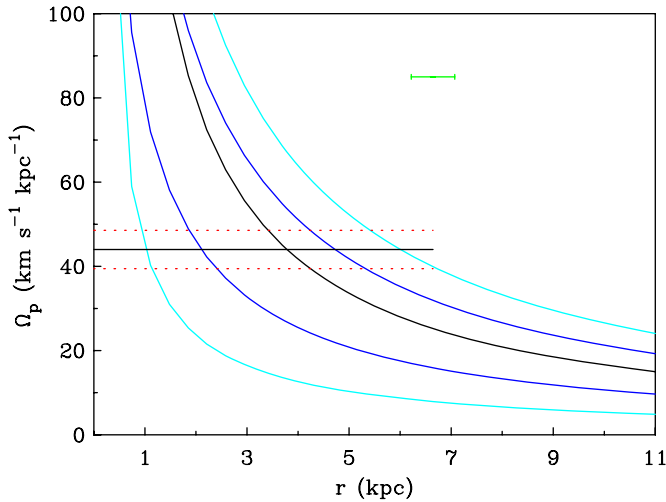
Figure 12. Best-fit regularized solution for NGC 3344 with $r_c = 6.8 \pm 0.43$ kpc for P.A. $= 155° \pm 2°$. For this solution, bins exterior to r_c (not shown) have been calculated without regularization. Dashed red lines and the green horizontal error bar represent the dispersion in the pattern speeds and r_c in solutions derived at the three P.A.s. The value in the zone of the bright spiral structure corresponds to $\Omega_{p,1} = 44 \pm 4$ km s^{-1} kpc^{-1} out to r_c. Curves for Ω, $\Omega \pm \kappa/2$, and $\Omega \pm \kappa/4$ are shown in black, cyan, and blue.

(A color version of this figure is available in the online journal.)

TWR solution may represent a measure of the rotation speed of such a halo, if the structure in the outer disk (which, extends further in H I than in the optical; van der Kruit & Shostak 1982) arises in the manner considered by Frenk et al. (1988). Currently, however, it is not clear that the structure in NGC 3938 is compatible with the strong two-armed patterns found in the simulations of Frenk et al. (1988).

Alternatively, the overall instability of the disk might be increased by a global mass asymmetry resulting from the $m = 1$ perturbation to the halo potential considered by Jog (1997, 2000, 2002), which is also a possible source of the ellipticity. This latter scenario seems to be compatible with other observable characteristics of this galaxy, like Tully et al. (1996) and Bournaud et al. (2005), we find the H I disk to be slightly lopsided toward the north, and this $m = 1$ asymmetry appears in the H I velocity field, as well. (As previously demonstrated with the Hα observations of Daigle et al. 2006, we measure a $\sim$10–20 km s^{-1} difference between the approaching and receding sides beyond $r \sim 11$ kpc.) In this case, the TWR measurement may reflect the response of the gas (and stars) to this perturbation if the elliptical orbits calculated by Jog (1997) precess with frequency $\Omega - \kappa/2$.

Again, our TWR measurement does not confirm, or distinguish between, these possibilities. In either of the two scenarios it is also not clear if, or how, the inner, higher speed may relate to the lower speed. Higher resolution observations are necessary to first establish which of the two solutions, Ω_p^A or Ω_p^B, is the most appropriate for this galaxy. Only then will it be possible to more rigorously explore the relation between the two-pattern speeds suggested by the solution Ω_p^B and perhaps then recognize the true nature of the low speed.

3.5. NGC 3344

The best-fit solution calculated in slices out to $|y| = 19.4$ kpc with radial bin width $\Delta r = 0.75$ kpc (corresponding to the $\sim 20''$ resolution of the H I cube) is shown in Figure 12 along with rotation and resonance curves. Immediately we notice that,

according to our determination of the cut radius $r_c = 6.8 \pm 0.43$ kpc—near the location where the warp has been identified to begin ($r \sim 7$ kpc; Verdes-Montenegro et al. 2000)—this spiral pattern ends at OLR, within the uncertainties. The inner bound for the single, constant speed $\Omega_p = 44 \pm 4$ km s^{-1} kpc^{-1} in Figure 12, on the other hand, is less clearly well established here. The paucity of 21 cm emission inside $r \sim 1$ kpc not only leads us to suspect that the measurement may not be valid all the way to the center, as suggested by our solution in Figure 12 (calculated with bins covering all radii $r \geqslant 0$), but it also prevents us from constraining the angular rotation curve there (and the position of the ILR) with confidence.

Even so, according to our estimate $r_{\text{ILR}} \sim 1.0$ kpc, the spiral could reasonably begin at the inner ring, as identified in the optical by Verdes-Montenegro et al. (2000). In this case, with the single-pattern speed implied by our TWR solution, both the inner and outer rings, at $r = 1$ kpc and $r = 7$ kpc (Verdes-Montenegro et al. 2000), are arguably associated with spiral's ILR and OLR. We note that this depends in no small part on the TWR method; the separation achieved by the cut radius between the strong spiral structure and the $m = 1$ distortion grants a measurement for the former constant speed which is significantly different from that implied by the traditional TW method, $\Omega_p = 26 \pm 6$ km s^{-1} kpc^{-1} (calculated with the same slices, kinematic parameters, and limits of integration as in the TWR calculation).

The model-independent TWR method, moreover, resolves the ambiguity in the study by Verdes-Montenegro et al. (2000). There, the uncertainty in the rotation curve precluded the reliable association of the inner and outer rings with resonances, and the estimation of a pattern speed (Verdes-Montenegro et al. 2000). With the identification above we can confirm that the outer pseudoring at $r \sim 7$ kpc originates with the spiral, as opposed to the bar, which Verdes-Montenegro et al. (2000) argue is too small to have an OLR at this radius.

The inner ring, on the other hand, seems more likely related to the bar (which it surrounds; Verdes-Montenegro et al. 2000), given the proximity of these two features. That we find the spiral's ILR nearly coincident with the location of the inner ring might then be a manifestation of resonance overlap between the speeds of the bar and spiral. If the spiral with lower speed is driven at resonance, for example, our TWR solution may suggest a reasonable speed for the bar, which we are prevented from measuring here. In particular, if we associate the inner, ILR ring with inner extent of the spiral (inside of which the H I density falls off), such a scenario could be realistically achieved via CR–ILR mode coupling, where the bar rotates with pattern speed $\Omega_p \gtrsim 150$ km s^{-1} kpc^{-1} for $r_{\text{CR}} \sim 1.0$ kpc. The bar, with length $a_B \sim 0.7$ kpc (Verdes-Montenegro et al. 2000), in this case would be reasonably fast, with $r_{\text{CR}}/a_B \sim 1.4$. Alternatively, we might expect a bar pattern speed $\Omega_p \gtrsim 80$ km s^{-1} kpc^{-1}, in the event of the CR-inner 4:1 resonance overlap discussed in Section 3.2, in which case $r_{\text{CR}}/a_B \sim 3.5$. In the former (latter) scenario, the inner ring could be located near the bar's CR (inner 4:1 resonance), at least with the rotation and resonance curves derived here.

Our TWR solution also seems to endorse the scenario speculated upon by Verdes-Montenegro et al. (2000) for the origin of the warp in this galaxy, namely, through the nonlinear coupling proposed by Masset & Tagger (1997a). In this scheme, the warp (manifest in the lopsided part of the H I distribution, which extends 34% further toward the SE than NW; Verdes-Montenegro et al. 2000) would originate through a coupling

at OLR between a spiral density wave and two "warp waves." Since we have established that the spiral structure ends at OLR, in the absence of tidal interaction with a companion galaxy (Thilker et al. 2007), the spiral pattern itself could be capable of generating the warp in the outer disk.

4. SUMMARY AND CONCLUSIONS

Direct pattern speed measurement affords an observational resolution for several fundamental issues in the nature and origin of spirals. The relation between bar and spiral pattern speeds, the number and radial domains of patterns speeds that can be sustained in the disk, and whether spiral structure is steady or winding, for example, can all be established with knowledge of spiral speeds and their radial variation. The TWR method, a technique for measuring radially varying pattern speeds, supplies us with the first such measurements to address these issues.

In this paper, we have applied the TWR method to observations of CO and H I in four spiral galaxies. For this work, we have expanded the number of spiral galaxies to which TW-type calculations can be applied by considering, for the first time, the combination of both molecular and atomic gas. Together, the two ISM phases better meet the continuity requirement of the method and also afford greater insight into whether (and how) multiple spiral pattern speeds extend over a large range of radii. This has notably increased the sample size of galaxies analyzed with the TWR method so far.

Our TWR solutions for M101 (Section 3.2), which, of all the solutions presented here, are equipped with the smallest radial bins, very clearly show radial variation in the pattern speed across the disk. Within the inner 3′, we find convincing evidence that the bar and spiral have the same pattern speed (distinct from an exterior speed), and that both lie inside corotation. This represents a scenario quite different from recent findings in favor almost exclusively of fast bars (with $1 \lesssim r_{CR}/a_b \lesssim 1.4$; Corsini 2008) albeit in mostly early-type barred galaxies.

In M101—as well as in IC 342 and possibly NGC 3938—we also find that the extensive spiral structure there is best described with more than a single-pattern speed. Furthermore, in both M101 and IC 342 we find evidence that the transition between two speeds coincides with resonance overlap. In the former, the transition between the two- and four-armed patterns occurs near the overlap of the inner's OLR and the outer's inner 4:1 resonance. In the latter case, the inner pattern transitions to a four-armed spiral at an OLR–ILR overlap.

Although the specific resonance overlaps identified in M101 and IC 342 have not been conclusively demonstrated as true instances of mode coupling (e.g., Sygnet et al. 1988; Masset & Tagger 1997b), together with the CR-inner 4:1 resonance overlap in M51 (Paper II), this work suggests that there exist several possibilities dictated by resonance overlap by which extensive spiral structure can be sustained. Our findings are qualitatively similar to the barred spiral simulations of Rautiainen & Salo (1999), but we note that the spatially coincident existence of multiple modes with different pattern speeds, as often found there beyond the bar, is untested with the TWR calculation here. Even so, the outer four-armed spirals in both M101 and IC 342 are arguably excited at resonance by the patterns interior.

On the other hand, in our sample we also find extensive spiral structure in the absence of clear resonance overlap. The speed characteristic of the outer, flocculent structure in NGC 3938, for instance, does not seem to be clearly related to that of the inner, two-armed spiral, if the two speeds are distinct. In addition, the

tight spiral structure throughout the H I emitting disk in NGC 3344 is best described with a single, constant pattern speed.

In no case do we find that pattern speed is a smoothly decreasing function of radius, as might be expected for a winding spiral. Our cut procedure, however, may introduce a bias against such spirals if they exist preferentially in the outer regions of the disks in our sample; the radial bins covering the outer portion of three of the four galaxies where a warp is evident are excluded from our models and calculated without regularization.

Even though in this case we cannot characterize the patterns that may distinguish the warped regions of the disks in our sample, accurate measurements for the pattern speeds of the structure interior can, themselves, recommend different mechanisms by which warps are expected to originate and evolve. The galaxies in this sample are consistent with various existing explanations. Where the spiral structure ends at OLR in a warped, isolated galaxy (e.g., NGC 3344), for example, spirals themselves may be capable of exciting the warp through the nonlinear coupling proposed by Masset & Tagger (1997a). In the absence of both a companion and this resonance boundary, but where the disk is intrinsically elliptical, as in NGC 3938, the ellipticity, the warp and/or the instabilities in the disk may arise with a DM halo or the asymmetric accretion of matter (discussed in Section 3.4). An obvious companion, on the other hand, is a clear, potential source of tidal perturbation to the disk (e.g., M101 and IC 342). Although an accompanying warp or distortion may not necessarily relate to the spiral structure at resonance, where the speed of outer structure is near the Ω-$\kappa/2$ curve, for example, this structure may be resonantly excited (at ILR) by the external perturber (see e.g., Salo & Laurikainen 2000).

These issues, and the existence of extensive spiral structure, are best developed with a larger sample of galaxies, where meaningful trends will be more clearly established. For greatest effect, the TWR calculation should be applied to higher resolution H I observations than we analyze here. In all of the galaxies in our sample (excepting M101), the resolution of the H I data limits our confidence in how well radial variation is constrained. It also inhibits our leverage on information extracted in the zone traced by CO emission (which we smooth to the resolution of the H I in combining the two observations).

A large radial bin width likewise prevents us from satisfactorily testing the effect of variation in the CO-to-H_2 conversion factor on TWR pattern speed estimates. Future studies with higher resolution observations (and therefore more radial bins across the CO-emitting disk) may be able to better test for the effects of a gradient or arm–interarm variations in X. We note, though, that these types of variations were found to have a negligible effect on TW estimates (Zimmer et al. 2004), and here we find that low-level variation in the X-factor produces very little change in our TWR solutions for M101.

In general, these types of TWR measurements in nearby galaxies are invaluable for interpreting observational studies of the evolution of bar and disk parameters now possible with HST. They also promise to be significant for studies at intermediate redshift, and future studies with JWST, which will extend structural parameter measurement to larger redshifts and allow smaller bars and the earlier evolution of disks to be studied.

REFERENCES

Andersen, D. R., Bershady, M. A., Sparke, L. S., Gallager, J. S., & Wilcots, E. M. 2001, ApJ, 551, L131
Arimoto, N., Sofue, Y., & Tsujimoto, T. 1996, PASJ, 48, 275
Bertin, G., Lin, C. C., Lowe, S. A., & Thurstans, R. P. 1989, ApJ, 338, 78
Boselli, A., Lequeux, J., & Gavazzi, G. 2002, A&A, 384, 33
Bournaud, F., Combes, F., Jog, C. J., & Puerari, I. 2005, A&A, 438, 507
Bureau, M., Freeman, K. C., Pfitzner, D. W., & Meurer, G. R. 1999, AJ, 118, 2158
Buta, R., & Combes, F. 1996, Fundam. Cosm. Phys., 17, 95
Castro-Rodriguez, N., & Garzon, F. 2003, A&A, 411, 55
Cedres, B., Urbaneja, M. A., & Cepa, J. 2004, A&A, 422, 511
Combes, F., & Becquaert, J.-F. 1997, A&A, 326, 554
Combes, F., & Elmegreen, B. G. 1993, A&A, 271, 391
Combes, F., & Gerin, M. 1985, A&A, 150, 327
Corsini, E. M. 2008, in IAU Symp. 245, Formation and Evolution of Galaxy Bulges, ed. M. Bureau, E. Athanassoula, & B. Barbuy (Cambridge: Cambridge Univ. Press), 125
Crosthwaite, L. P., Turner, J. L., & Ho, P. T. P. 2000, AJ, 119, 1720
Crosthwaite, L. P., Turner, J. L., Hurt, R. L., Levine, D. A., Martin, R. N., & Ho, P. T. P. 2001, AJ, 122, 797
Daigle, O., Carignan, C., Amram, P., Hernandez, O., Chemin, L., Balkowski, C., & Kennicutt, R. 2006, MNRAS, 367, 469
Debattista, V. P. 2003, MNRAS, 342, 1194
Debattista, V. P., Mayer, L., Carollo, C. M., Moore, B., Wadsley, J., & Quinn, T. 2006, ApJ, 645, 209
Debattista, V. P., & Sellwood, J. A. 2000, ApJ, 543, 704
Dubinski, J., Berentzen, I., & Shlosman, I. 2009, ApJ, 697, 293
Dubinski, J., & Carlberg, R. G. 1991, ApJ, 378, 496
Elmegreen, B. G., Elmegreen, D. M., Chromey, F. R., Hasselbacher, D. A., & Bissell, B. A. 1996, AJ, 111, 2233
Elmegreen, B. G., Elmegreen, D. M., & Montenegro, L. 1992, ApJS, 79, 37
Elmegreen, B. G., Elmegreen, D. M., & Seiden, P. E. 1989, ApJ, 343, 602
Faber, S. M., & Gallagher, J. S. 1979, ARA&A, 17, 135
Frenk, C., S., White, S. D. M., Davis, M., & Efstathiou, G. 1988, ApJ, 327, 507
Garcia-Burillo, S., Combes, F., & Gerin, M. 1993, A&A, 274, 148
Helfer, T. T., Thornley, M. D., Regan, M. W., Wong, T., Sheth, K., Vogel, S. N., Blitz, L., & Bock, D. C.-J. 2003, ApJS, 145, 259
Henry, A. L., Quillen, A. C., & Gutermuth, R. 2003, AJ, 126, 2831
Huchtmeier, W. K., & Witzel, A. 1979, A&A, 74, 138
Hunter, S. D., et al. 1997, ApJ, 481, 205
Ideta, M. 2002, ApJ, 568, 190
Jimenez-Vicente, J., Battaner, E., Rozas, M., Castaneda, H., & Porcel, C. 1999, A&A, 342, 417
Jog, C. J. 1992, ApJ, 390, 378
Jog, C. J. 1997, ApJ, 488, 642
Jog, C. J. 2000, ApJ, 542, 216
Jog, C. J. 2002, A&A, 391, 471
Jurcevic, J. S., & Butcher, D. 2006, A&AS, 208, 1303
Kamphuis, J. 1993, PhD thesis, Univ. of Groningen
Kenney, J. D. P., Scoville, N. Z., & Wilson, C. D. 1991, ApJ, 366, 432
Knapen, J. H., Beckman, J. E., Cepa, J., & Nakai, N. 1996, A&A, 308, 27

Korchagin, V., Orlova, N., Kikuchi, N., Miyama, S. M., & Moiseev, A. 2005, arXiv:astro-ph/0509708v1
Kormendy, J., & Norman, C. A. 1979, ApJ, 233, 539
Lin, C. C., & Shu, F. H. 1964, ApJ, 140, 646
Martinez-Garcia, E. E., Gonzalez-Lopezlira, R. A., & Bruzual-A, G. 2009, ApJ, 694, 512
Masset, F., & Tagger, M. 1997a, A&A, 318, 747
Masset, F., & Tagger, M. 1997b, A&A, 322, 442
Meidt, S. E., Rand, R. J., Merrifield, M. R., Debattista, V. P., & Shen, J. 2008a, ApJ, 676, 899
Meidt, S. E., Rand, R. J., Merrifield, M. R., Shetty, R., & Vogel, S. 2008b, ApJ, 688, 224
Merrifield, M. R., Rand, R. J., & Meidt, S. E. 2006, MNRAS, 366, 17
Petitpas, G. R., Das, M., Teuben, P. J., & Vogel, S. N. 2004, in IAU Symp. 220, Dark Matter in Galaxies, ed. S. D. Ryder et al. (Dordrecht: Kluwer), 277
Quillen, A. C., Frogel, J. A., Kenney, J. D. P., Pogge, R. W., & Depoy, D. L. 1995, ApJ, 441, 549
Rand, R. J. 1993, ApJ, 404, 593
Rand, R. J., & Wallin, J. F. 2004, ApJ, 614, 142
Rautiainen, P., & Salo, H. 1999, A&A, 348, 737
Rautiainen, P., & Salo, H. 2005, ApJ, 631, L129
Rautiainen, P., Salo, H., & Buta, R. 2004, MNRAS, 349, 933
Rautiainen, P., Salo, H., & Laurikainen, E. 2008, MNRAS, 388, 1803
Regan, M. W., Sheth, K., Teuben, P. J., & Vogel, S. N. 2002, ApJ, 574, 126
Rownd, B. K., Dickey, J. M., & Helou, G. 1994, AJ, 108, 1638
Salo, H., & Laurikainen, E. 2000, MNRAS, 319, 393
Sellwood, J. A. 2008, ApJ, 679, 379
Sellwood, J. A., & Carlberg, R. G. 1984, ApJ, 282, 61
Sellwood, J. A., & Kahn, F. D. 1991, MNRAS, 250, 278
Sellwood, J. A., & Sparke, L. S. 1988, MNRAS, 231, 25
Sygnet, J. F., Tagger, M., Athanassoula, E., & Pellat, R. 1988, MNRAS, 232, 733
Thilker, A., et al. 2007, ApJS, 173, 538
Thomasson, M., Elmegreen, B. G., Donner, K. J., & Sundelius, B. 1990, ApJ, 356, 9
Tremaine, S., & Weinberg, M. D. 1984, ApJ, 282, L5
Tully, R. B., Verheijen, M. A. W., Pierce, M. J., Huang, J.-S., & Wainscoat, R. J. 1996, AJ, 112, 2471
van der Hulst, J. M., Terlouw, J. P., Begeman, K. G., Zwitser, W., & Roelfsema, P. R. 1992, in ASP Conf. Ser. 25, Astronomical Data Analysis Software and Systems I, ed. D. M. Worrall, C. Biemesderfer, & J. Barnes (San Francisco, CA: ASP), 131
van der Kruit, P. C., & Shostak, G. S. 1982, A&A, 105, 351
Verdes-Montenegro, L., Bosma, A., & Athanassoula, E. 2000, A&A, 356, 827
Vila-Costas, M. B., & Edmunds, M. G. 1992, MNRAS, 259, 121
Waller, W. H., et al. 1997, ApJ, 481, 169
Walter, F., Brinks, E., de Blok, W. J. G., Bigiel, F., Kennicutt, R. C., & Thornley, M. D. 2008, AJ, 136, 2563
Weinberg, M. D. 1985, MNRAS, 213, 451
Weinberg, M. D., & Katz, N. 2007, MNRAS, 375, 460
Westpfahl, D. J. 1998, ApJS, 115, 203
Wong, T., & Blitz, L. 2002, ApJ, 569, 157
Zimmer, P., Rand, R. J., & McGraw, J. T. 2004, ApJ, 607, 285